11

Ultrasonic Additive Manufacturing: Microstructural and Mechanical Characterization

Tianyang (Tyler) Han, Leon M. Headings, and Marcelo J. Dapino

Department of Mechanical and Aerospace Engineering, The Ohio State University, Columbus, OH 43210, USA

11.1 Introduction

Ultrasonic additive manufacturing (UAM), also called ultrasonic consolidation, is a solid-state process that combines ultrasonic metal welding of foil feedstock with subtractive machining to build near-net shape parts [1]. Metal foil layers are welded using a rolling sonotrode to apply ultrasonic (∼20 kHz) transverse vibrations in combination with a normal force. This creates localized plastic deformation at the weld interface that collapses asperities and disperses oxides and contaminants, resulting in nascent metal surfaces that produce gapless metallurgical bonds. Components are built up by repeating this welding process next to, or on top of, the previous layer of foil. Normal force, vibration amplitude, weld speed, and baseplate temperature are the key parameters used to control the UAM process [2]. In order to create internal features or embed structural or active materials such as reinforcement fibers [3, 4], thermally sensitive materials like nickel-titanium shape memory alloys [5, 6], and fiber optics [7], an integrated computer numerical control (CNC) system is used to machine cavities and features before welding additional layers of foil over the top. The CNC system can also serve to machine parts to final dimensions after welding is completed.

The solid-state nature of the UAM process is a key feature that enables the embedment of thermally sensitive materials and sensors. It also allows the joining of dissimilar materials, such as Al-Ti [8, 9] and Al-ceramic [10], without creating brittle phases. Measurements have shown that UAM welding typically occurs at less than one-half of the melting temperature of the constituent materials [11].

11.2 Microstructure Analysis of UAM Builds

Global and local changes in the microstructure of UAM samples are typically investigated using microstructural analysis techniques such as optical imaging, scanning electron microscopy (SEM) including electron backscatter diffraction

Solid-State Metal Additive Manufacturing: Physics, Processes, Mechanical Properties, and Applications, First Edition. Edited by Hang Z. Yu, Nihan Tuncer, and Zhili Feng.

(EBSD), transmission electron microscopy (TEM), and energy-dispersive X-ray spectroscopy (EDS). To maintain the integrity of the microstructures formed during the UAM process, the samples undergo a sectioning procedure using a low-speed saw equipped with coolant to minimize heat generation. Subsequently, the samples are embedded in conductive bakelite material and undergo polishing following established metallography preparation protocols.

11.2.1 Similar Material Joining with UAM

UAM has been demonstrated to produce robust metal builds in similar materials such as Al to Al [12, 13], Cu to Cu [14], and steel to steel [15, 16]. The UAM interface of these materials has similar grain structures and textures. This section uses a recent study of UAM steel welding [12] as an example. In this study, to investigate the influence of baseplate temperature and hot isostatic pressing (HIP) on mechanical properties of UAM stainless steel (SS) 410 builds, samples were analyzed with both SEM and EBSD. Figure 11.1a,c present backscattered electron (BSE) micrographs demonstrating that the interface (indicated by black arrows) of the as-welded UAM SS 410 primarily comprises ferrite grains. The analysis of Figure 11.1b,d will be addressed in the last paragraph of this section.

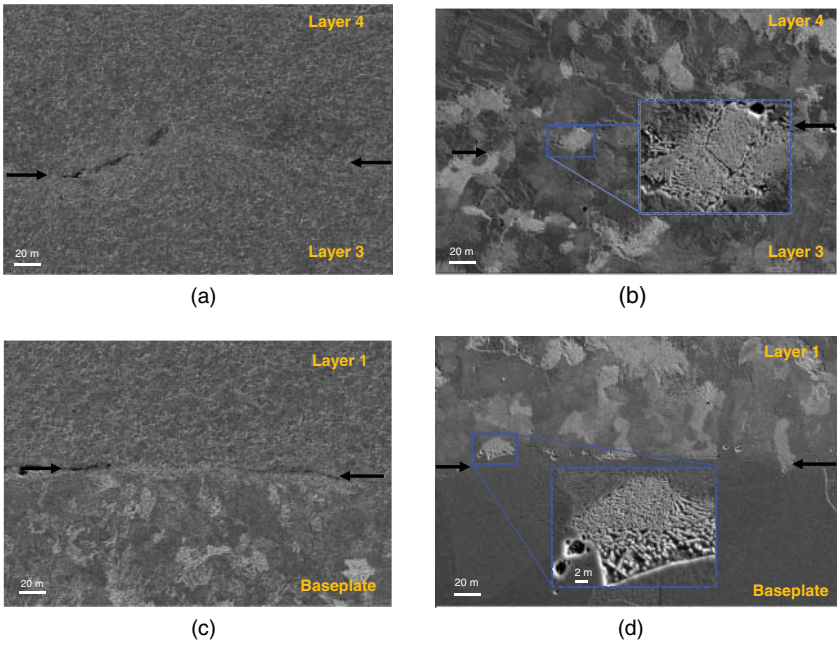

Figure 11.1 The backscattered electron micrographs of UAM interfaces for SS 410 are presented as follows: (a) as-welded interface between the 3rd and 4th foils, (b) post-HIP interface between the 3rd and 4th foils, (c) as-welded interface between the baseplate and the 1st foil, and (d) post-HIP interface between the baseplate and the 1st foil. Source: Reproduced with permission from Han et al. [17]/Elsevier.

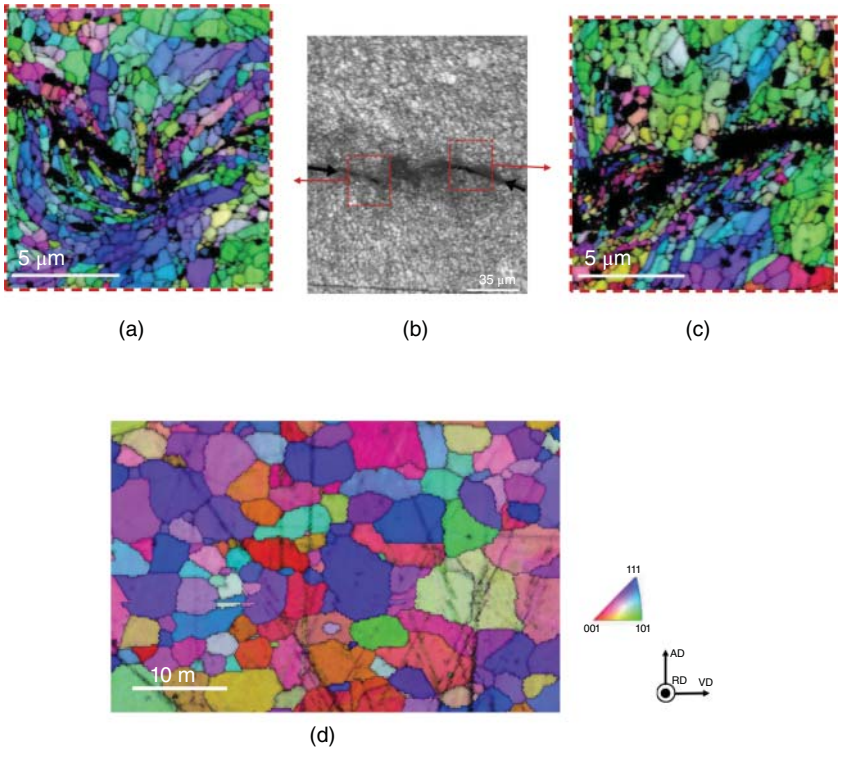

Figure 11.2 EBSD micrographs of the following are presented: (a) bonded area, (b) UAM interface, (c) unbonded area, and (d) as-received SS 410 foil. It is noted that SEM micrographs, which are not provided here, were used to distinguish bonded areas from unbonded areas. Small black dots observed in (a) and (c) are unresolved due to either their small size or distorted grain structure. In (a), the black distorted regions located in the central part indicate significant plastic deformation, resulting in zones with low image quality. Conversely, the black zones observed in the central part of (c) represent voids. Source: Reproduced with permission from Han et al. [17]/Elsevier.

Figure 11.2 shows EBSD micrographs of both bonded and unbonded regions at the same interface. Figure 11.2b displays the image quality mapping, while Figure 11.2a,c overlay the inverse pole figure (IPF) with the image quality mapping. The coordinate system is defined as the accumulating direction (AD), vibrating direction (VD), and rolling direction (RD) [18]. Figure 11.2d shows the EBSD of the SS 410 foil in the as-received state, revealing a grain structure that is equiaxed. Following the UAM process, both bonded and unbonded areas at the interface exhibit highly deformed grains.

The microtexture depicted in Figure 11.3 reveals the presence of a pronounced alpha fiber <110>‖VD. The absence of other variants, particularly Goss variants, suggests that the formation of new grains at the UAM interface is not attributable to nucleation and growth but rather evolves through plasticity within the shear region [19]. This observation aligns with a comparable alpha texture <110>‖VD observed in the interstitial-free steel sample subjected to high strain rate deformation [19].

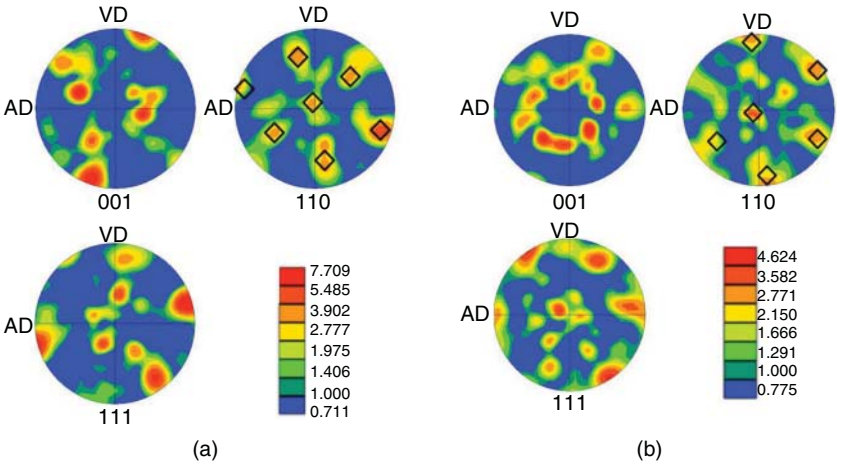

Figure 11.3 The pole figures reveal an identical alpha fiber texture, indicating that the transformation from BCC to FCC did not occur during the UAM process. Specifically, (a) represents the microtexture of the unbonded area, while (b) showcases the microtexture of the bonded area. Source: Han et al. [17] Reproduced with permission from Elsevier.

The resemblance in texture patterns indicates that both the bonded and unbonded areas of the UAM interface likely underwent significant deformation at high strain rates. The unbonded area is hypothesized to be a zone where excessive plastic deformation breaks the previously established bonds.

To investigate the effect of HIP on microstructure alterations, SEM and EBSD analyses were conducted on samples prepared at a baseplate temperature of 204 °C. In a previous study examining the UAM of carbon steel 4130 [20], the UAM interfaces were primarily composed of ferrite. The authors hypothesized that the presence of nonmetallic inclusions at the interface facilitated ferrite nucleation while impeding pearlite formation. However, the interfaces of UAM SS 410 samples subjected to HIP exhibited a pearlite composition, as depicted in Figure 11.1b,d. Moreover, the significant grain growth at the interface suggests that oxide particles cause pinning in aluminum but not in steel [21]. Given the prolonged exposure time and slow cooling rates employed in this study, the foil-to-foil interface is predominantly characterized by pearlite, as shown in Figure 11.1b, with localized pockets of martensite.

11.2.2 Dissimilar Material Joining with UAM

11.2.2.1 Al-Ceramic Weld

An example of Al 6061-ceramic welding achieved by UAM is shown in Figure 11.4. This type of metal-to-ceramic weld can also be achieved through fusion-based welding. However, the strength of the metal-to-ceramic interface achieved by UAM is 72 MPa, which is higher than the strength achieved by fusion-based welding [22]. As the joints cool down from the melting point (T_m) to room temperature in fusion welding, large residual stress is found at the metal-to-ceramic weld interface due to

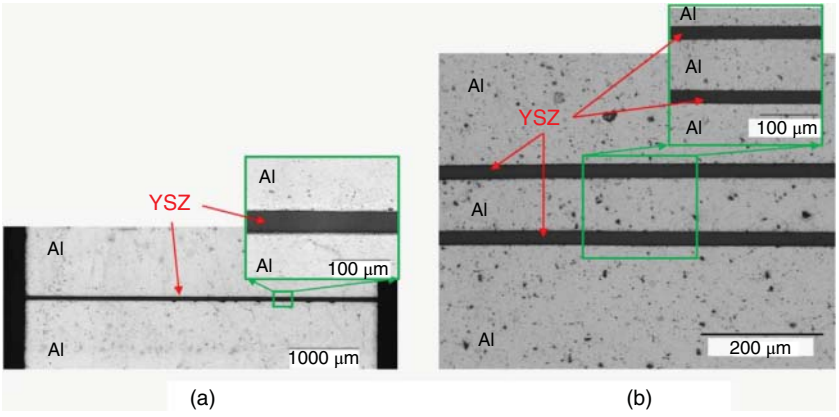

Figure 11.4 (a) Optical micrograph across the width of the Yttria-stabilized zirconia (YSZ) to Al welding interface on an as-welded shear sample and (b) optical micrograph showing two layers of YSZ films welded within an Al structure. Source: Reproduced with permission from Deng et al. [10]/Elsevier.

the difference in coefficients of thermal expansion. Higher temperature ($>T_m$) and longer welding duration (minutes or hours) are also required for fusion-based welding, as compared to lower baseplate temperature (typically $<0.5\ T_m$) and shorter welding duration (~60 ms) for UAM [10].

11.2.2.2 Ni-Steel Weld

In a recent study by Kuo et al. [11], a method to achieve UAM steel-steel welds with Ni interlayers was proposed. The concept is to use interlayers between the steel layers and then dissolve the interlayer material into the steel layers with a post-weld heat treatment (PWHT). A thermodynamic calculation was performed using THERMO-CALC and DICTRA to simulate the post-weld heat treatment. A PWHT temperature of 1000 K and a holding time of 1 hour, 2 hours, and 10 hours were selected for experimental validation. Microstructural analyses were done by optical imaging, SEM, and EBSD for UAM 4130 with and without Ni interlayers. As presented in Figure 11.5, bonded and unbonded zones were identified at the interface of as-welded UAM 4130 without a Ni interlayer. The unbonded zone is formed due to the lack of plastic deformation, which is confirmed by the higher magnification image shown in Figure 11.5c. In contrast, the bonded zone is formed due to extensive plastic deformation, which can be inferred from the decomposition of cementite laths near the interface, as shown in Figure 11.5d.

SEM images of a weld interface of UAM 4130 with Ni interlayer are presented in Figure 11.6. Fewer voids and non-uniform grain refinement were found at the Ni-steel interface. Grain refinement is found to be more pronounced in the rough surface region where the Ni flows along the contours of the steel, as shown in Figure 11.6a. On the other hand, less refinement was found near the flat surface region, as shown in Figure 11.6c.

Further EBSD analyses are presented in Figure 11.7. The ferrite grains at the interfaces in the as-welded UAM 4130 without Ni interlayers are much finer compared

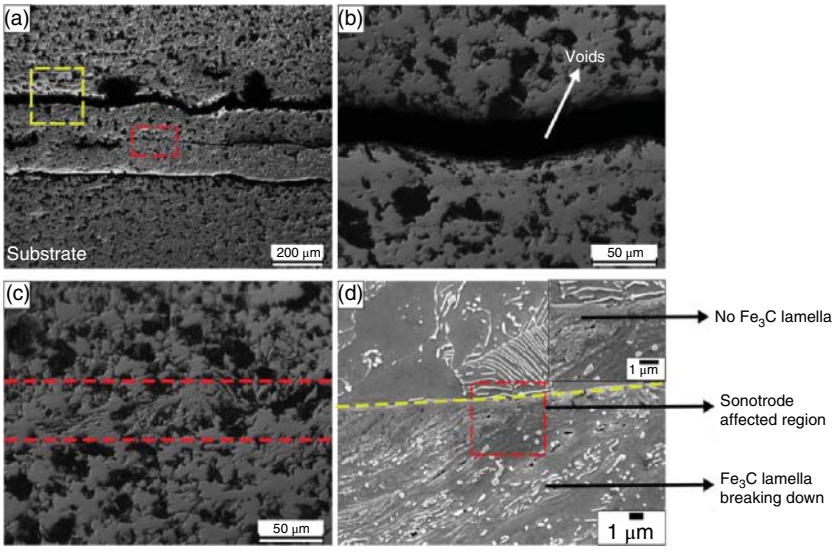

Figure 11.5 Optical image of (a) welding interface of as-welded UAM 4130 without Ni interlayers, (b) unbonded region at a higher magnification, (c) bonded region at a higher magnification, and (d) SEM image of the bonded region. Source: Reproduced with permission from Kuo et al. [11]/Taylor & Francis.

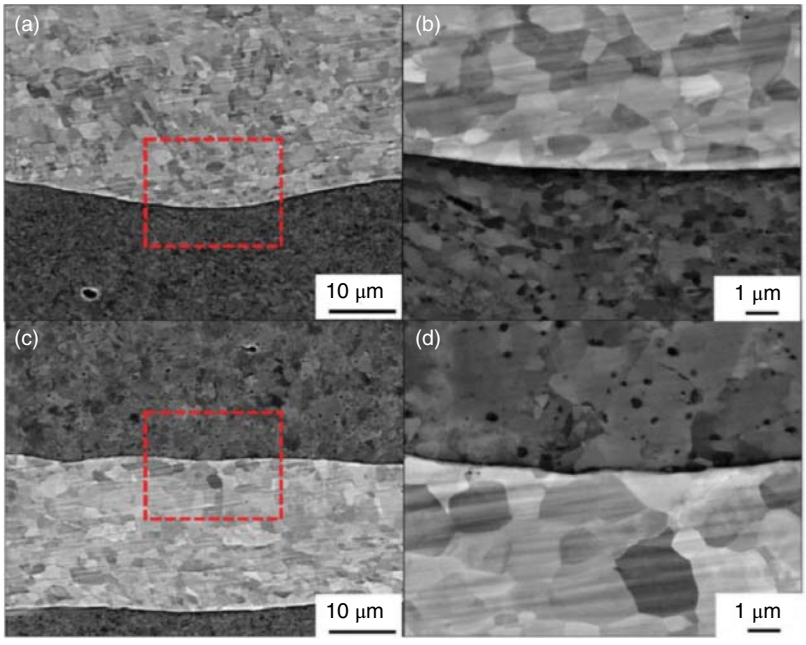

Figure 11.6 SEM images of the welding interface of as-welded UAM 4130 with Ni interlayers: (a) rough steel interface area at a lower magnification, (b) rough steel interface area at a higher magnification, (c) flat steel interface area at a lower magnification, and (d) flat steel interface area at a higher magnification. Source: Reproduced with permission from Kuo et al. [11]/Taylor & Francis.

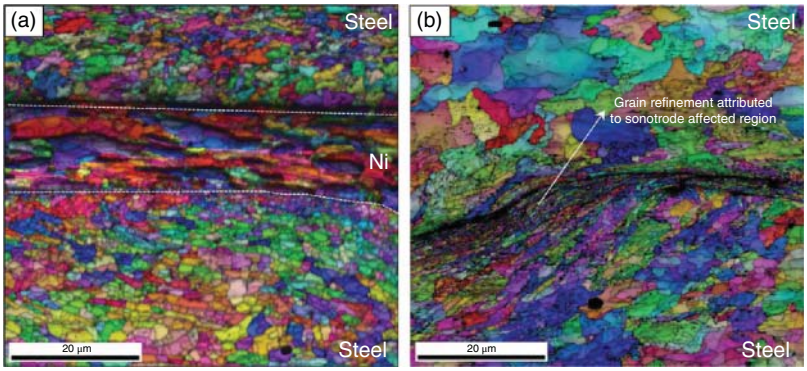

Figure 11.7 EBSD of the interface of (a) as-welded UAM 4130 with Ni interlayers and (b) as-welded UAM 4130 without Ni interlayers. Source: Reproduced with permission from Kuo et al. [11]/Sage Publications.

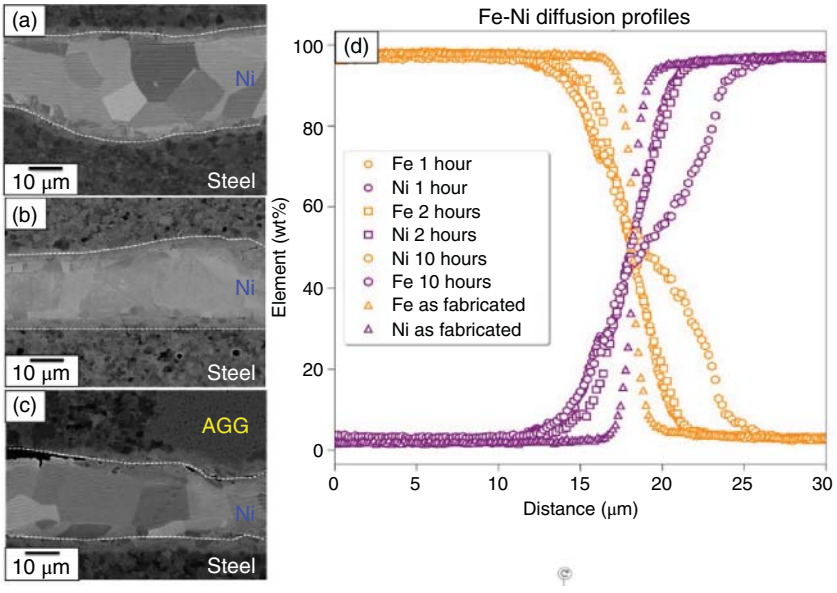

Figure 11.8 SEM images of the UAM Ni-steel welding interfaces after heat treatment at 1000 K for (a) 1 hour, (b) 2 hours, (c) 10 hours, and (c) EDS line scans of inter-diffusion zones of Fe (purple) and Ni (orange) in the as-welded and PWHT samples. Source: Reproduced with permission from Kuo et al. [11]/Taylor & Francis.

to the as-welded UAM 4130 with Ni interlayers. This reduction in grain size may result from the higher power input applied to the UAM steel samples without Ni interlayers.

Micrographs of the heat-treated and as-welded samples with Ni interlayers are presented in Figure 11.8. The SEM images show contrast at the Ni-Fe interfaces, which indicates the inter-diffusion of Ni into steel. In addition, there is a zone in the steel adjacent to the Ni foil showing a different contrast, which is attributed to

the formation of an FCC layer. Even though significant grain growth in the Ni layer occurred during the heat treatment, the grain growth in the FCC zone was limited. The extent of the inter-diffusion is measured using EDS. As presented in Figure 11.8, the EDS micrographs show an inter-diffusion zone of about 10 μm for the sample which has been treated for 10 hours. This indicates that a Ni interlayer with a thickness <10 μm may completely dissolve in the steel, leading to the formation of a steel-steel bonding interface.

11.3 Hardness Analysis of UAM Builds

Microhardness and nanohardness tests are also being used to characterize the hardness changes during UAM and post-process treatment. In a recent study [17], microhardness tests were performed on cross-sectional samples of as-welded and HIP-treated UAM stainless steel 410, employing a grid pattern that spanned the thickness of the samples. The findings indicate that the overall hardness of the samples increased from 204 ± 7 HV in the as-welded condition to 240 ± 16 HV in the UAM with HIP condition, attributed to the formation of martensite. However, the entire cross-section did not undergo a complete transformation to martensite, primarily due to the relatively slow cooling rates ranging from 2 to 4 °C/min during the HIP process.

In order to further examine the effect of the UAM process on microstructure, nanoindentation tests were conducted to assess the localized hardness across the interface. Figure 11.9 demonstrates that the upper region of layer n exhibits greater hardness compared to the lower region of layer $n+1$ in the as-welded UAM steel samples. The enhanced hardness at the top of layer n is a result of severe plastic deformation caused by direct contact with the textured sonotrode. During the welding of layer $n+1$, the increased hardness in layer n is believed to restrict the amount

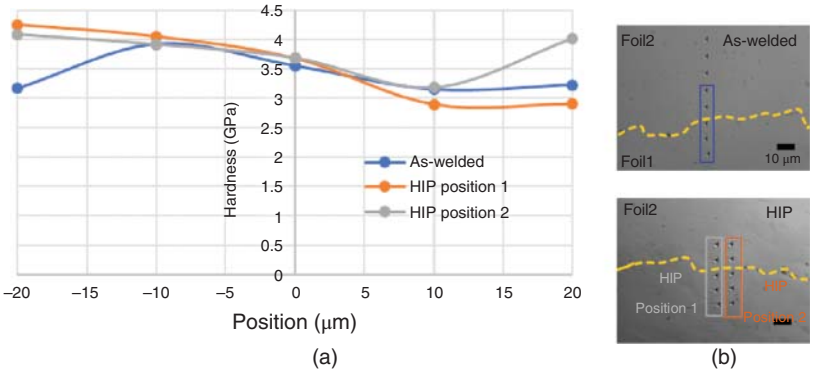

Figure 11.9 (a) Hardness maps obtained through nanoindentation were generated for the foil-to-foil interface at 0 μm for both the as-welded and post-HIP UAM samples. (b) Corresponding positions of the indentations. Source: Reproduced with permission from Han et al. [17]/Elsevier.

of plastic deformation and hinder the collapse of surface irregularities, potentially contributing to the formation of voids at the weld interface. The nanoindentation findings also indicate that the interface experiences more pronounced hardening. Notably, detailed microstructure characterization reveals no evidence of martensitic transformation, suggesting that the hardness increase at the interface primarily stems from grain boundary strengthening.

The effect of HIP on interfacial hardness was also examined. The hardness measured around the post-HIP foil-to-foil interface was approximately 3.68 GPa, whereas the hardness observed around the as-welded foil-to-foil interface was approximately 3.55 GPa. The load versus displacement curves obtained from both the as-welded and post-HIP samples show a similar pattern, wherein the upper region of layer n exhibited higher hardness compared to the lower region of layer $n + 1$. It is noted that the hardness increase observed above the interface in certain post-HIP regions could be attributed to the indentation of martensite pockets. The nanoindentation results from the selected regions aligned with the microhardness findings, indicating that the post-HIP samples exhibit higher hardness compared to the as-welded samples.

11.4 Mechanical Characterization of UAM Builds

Even though many mechanical test methods have been employed to characterize UAM-made materials, there are no existing standards. Since the UAM-fabricated builds have a unique laminated construction, quantification of the interfacial strength between layers is critical to understanding the strength of entire UAM structures. In previous UAM research, peel testing [23, 24] has been used to provide comparative interfacial strength information. This test is easy to conduct, but the test results cannot be compared with bulk material properties; it also does not do well enough to break a strong bond. Push-pin testing [25] is another testing method that provides comparative interfacial strength information. However, the test cannot provide material properties to benchmark against bulk material. Test specimens for push-pin testing require more material. The Z-tensile test has also been used to assess the weld quality of UAM builds. However, Z-tensile tests cannot measure the strength of a specified interface, and it takes more time to build specimens with the required height [12].

Based on the shortcomings of other types of tests, a new method was developed to characterize the mechanical strength of a specific interface of UAM builds. Shear testing was selected due to its ability to provide absolute interfacial strength information that could be benchmarked against bulk material. Shear tests can be classified as direct transverse shear or pure torsional shear, depending on the way that the shearing load is applied. Torsional shear tests are commonly used to characterize the shear behavior and properties of materials but cannot be used to test the strength of a specified interface. Therefore, the transverse shear test, which provides an approximate measurement of the shear strength of the material, was selected for testing of UAM samples. There are a number of transverse shear tests in the literature such as the double-notch shear test [26] and the Iosipescu test [27, 28]. However, mixed

failure modes are often reported for double-notch shear tests where the crack does not always propagate along the desired interface. The Iosipescu test requires a sample height that is 30 times the typical height of a UAM steel build. Hence, a custom shear test method was developed. This test method allows localized characterization of a specified interface at different regions of a UAM build. This shear test was first introduced by Wolcott et al [9] and has already been adopted in several UAM studies [15–17, 20]. The development, validation, and analysis of this method are summarized and presented in this chapter. The shear test method was first validated with bulk cast Al materials. Then, a finite element (FE) model was built to understand the influence of different shapes and dimensions including cuboid and stepped sample geometries on the shear test results. Finally, the shear test method was applied to UAM-made Al and steel samples.

11.4.1 Design of a Custom Shear Testing Method

A schematic of the shear fixture is shown in Figure 11.10a. The fixture is composed of two identical "L" shaped shearing blocks and two identical shearing plates. Shearing blocks are made of 4130 steel, and each of them is assembled with two steel pins and two copper bushings, as shown in Figure 11.10b. Shearing plates are made of heat-treated S7 tool steel. The UAM shear sample is placed into the slots in the shearing plates, as presented in Figure 11.10c. During testing, the shearing blocks are pressed by the compression platens of a load frame, as shown in Figure 11.10d. The shearing blocks then slide together to shear the sample at the interface between the shearing plates.

The shear strength, denoted as $\tau = F/A$, is determined by dividing the maximum compression force applied to the fixture during the shear testing process (measured using the load frame) by the initial cross-sectional area of the sample loaded in shear (measured using a micrometer).

11.4.2 Validation of the Shear Test

Bulk Al 6061 T6 with a known shear strength [29] was tested to verify the accuracy of the shear test method. The nominal width of a shear sample is fixed at 4.95 mm (0.195 in.). As shown in the schematic in Figure 11.11a, a shear sample with a length of 4.95 mm (0.195 in.) and a height of 3.25 mm (0.128 in.) is defined as a full-sized cuboid sample. Figure 11.11b shows a shear sample with a length of L that is smaller than 4.95 mm and a height of H that is no larger than 3.25 mm, which is defined as a stepped sample. The designated shearing interfaces are marked with solid black lines. The expectation is that the stepped sample may provide a more accurate and reliable measurement than the cuboid sample because the travel distance is shorter, and a lower bending moment is anticipated. To verify this assumption, full-sized cuboid samples as well as stepped samples with an arbitrary width of 2.24 mm and a full height of 3.25 mm, are machined from Al 6061 T6. The test was then conducted on five samples for each geometry. A summary of the shear test results for both geometries is provided in Table 11.1. Individual stress curves are presented in

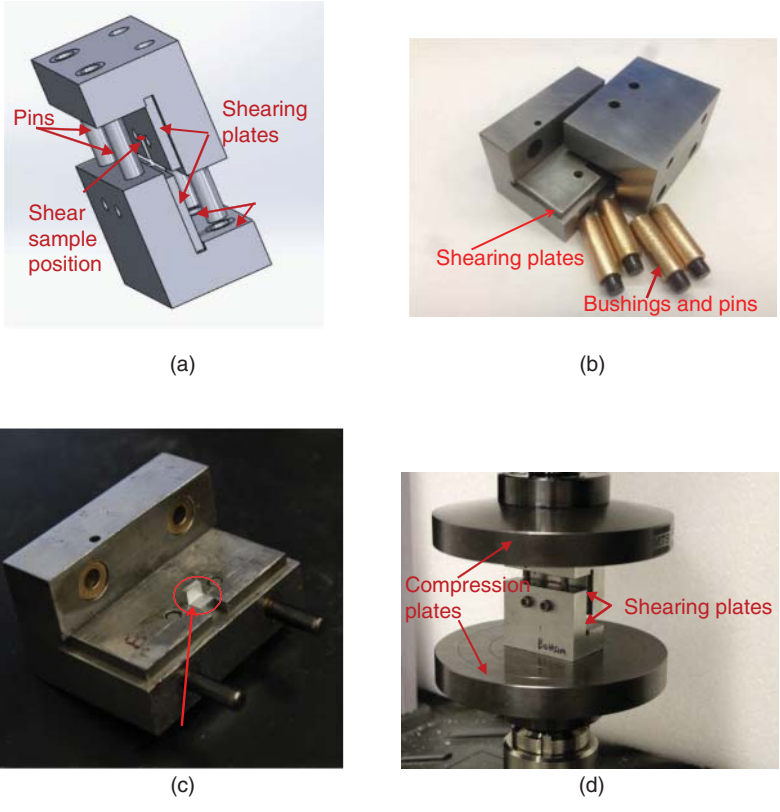

Figure 11.10 Shear test design including (a) conceptual schematic of shear fixture, (b) image of disassembled parts, (c) half of the shear fixture with loaded shear sample, and (d) experimental setup of the shear test with loaded sample. Source: Han [2]/from PhD dissertation.

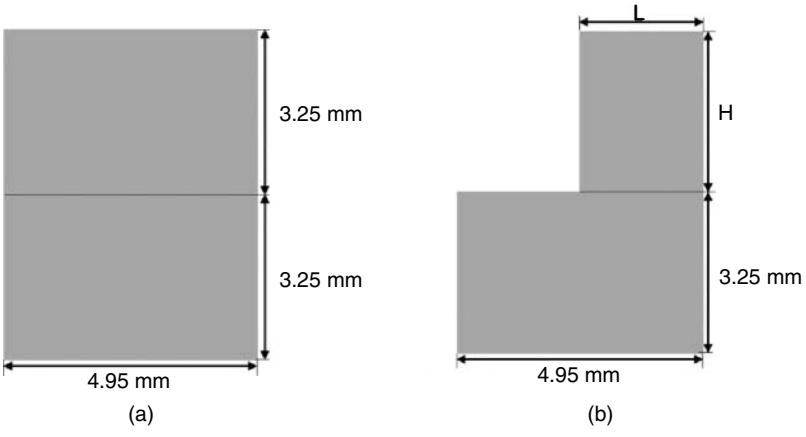

Figure 11.11 Schematics of (a) cuboid sample and (b) stepped sample. The desired shearing interfaces are marked with solid black lines. The depth of the samples is 4.95 mm. Source: Han [2]/from PhD dissertation.

Table 11.1 Shear strength of bulk Al 6061 T6.

Sample	Shear strength of cuboid samples (MPa)	Shear strength of stepped samples (MPa)
1	238.0	220.8
2	231.6	205.8
3	228.9	205.2
4	231.5	208.7
5	233.2	218.8
Average	232.6	211.9
Reference [29]	207	207

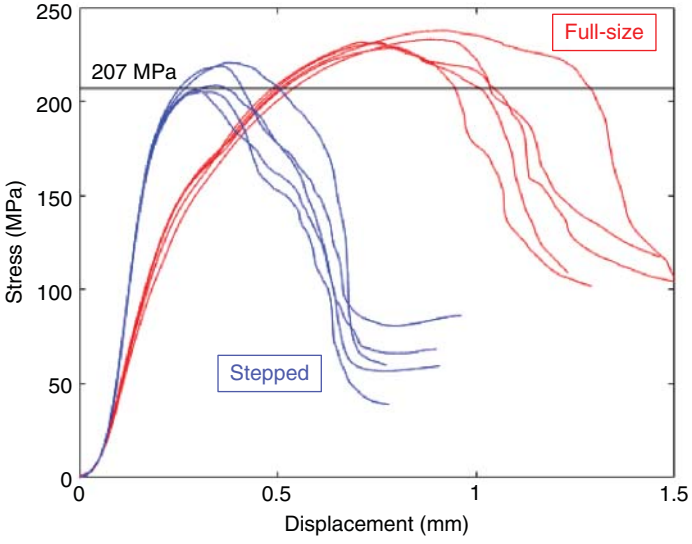

Figure 11.12 Individual stress versus displacement curves of full-sized cuboid and stepped samples with the reference value plotted as a solid black line. Source: Han [2]/from PhD dissertation.

Figure 11.12, with the reference value indicated by a solid black line. As shown, the testing of the stepped condition gives a shear strength measurement of 211.9 MPa, which is a 2.3% overestimation compared to the reference value of 207 MPa. By contrast, the testing of full-sized samples generates a measurement of 232.6 MPa, which is a larger overestimation of 12.4%.

11.4.3 Finite element Modeling of the Shear Test

To further understand the physical meaning of the stress curve and estimate the stress distribution in the shear sample, a two-dimensional FE model was developed

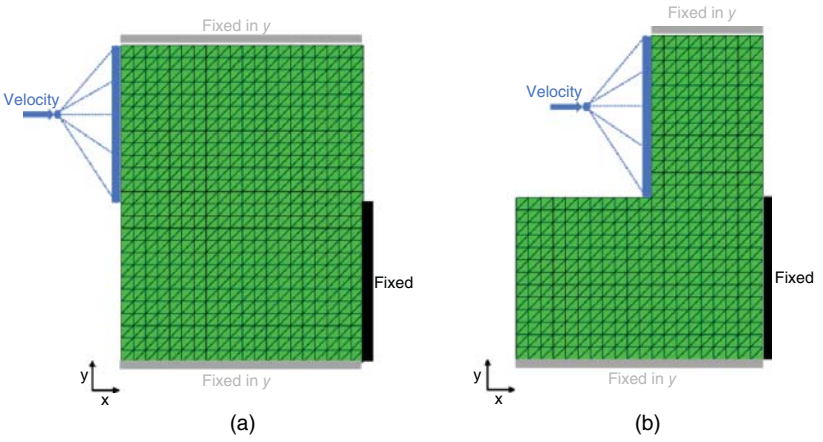

Figure 11.13 Boundary conditions and mesh details of (a) cuboid sample and (b) stepped sample. Source: Han [2]/from PhD dissertation.

in Abaqus. The mesh details and boundary conditions of the model are shown in Figure 11.13. Triangular elements are used in this study due to better performance during element deletion caused by shear damage. The mesh is iteratively refined until the balance between convergence and the peak load variation is reached. The bottom half of the right surface of the material is fixed. A boundary velocity of 0.02 mm/s is applied to a virtual control point, as shown in Figure 11.13. Then, a structural distributing coupling is defined between the point and the top half of the left surface. The motion defined on the point is used to simulate the compression from the load frame. The top and bottom surfaces of the material are constrained in the y direction. The shear stress is calculated as $\tau = F_r/A_e$, where F_r is the reaction force applied on the fixture, and A_e is the effective shearing area.

The elasticity and plasticity of Al 6061 T6 are used to define the material. The model presumes that the equivalent plastic strain at the damage $\bar{\varepsilon}_S^{pl}$ is defined as a function of the shear stress ratio θ_S and strain rate $\dot{\varepsilon}^{pl}$ [30]. The criterion for shear damage initiation is satisfied when

$$\omega_s = \int \frac{d\bar{\varepsilon}^{pl}}{\bar{\varepsilon}_S^{pl}(\theta_S, \dot{\varepsilon}^{pl})} = 1$$

where ω_S is a state variable that increases proportional to the incremental change in equivalent plastic strain. In this study, the shear damage properties for Al 6061 T6 are calibrated from an iterative process and defined as presented in Table 11.2.

Table 11.2 Shear damage properties used for modeling Al 6061 T6.

Fracture strain $\bar{\varepsilon}^{pl}$	Shear stress ratio θ_S	Strain rate $\dot{\varepsilon}^{pl}$
0.1	0.33	2

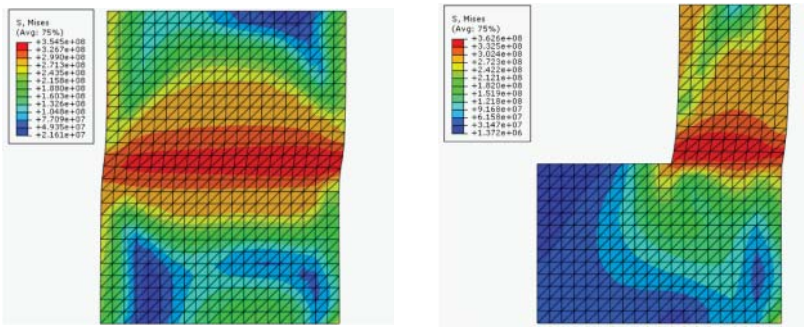

Figure 11.14 Stress distribution map of (a) cuboid sample and (b) stepped sample. Source: Han [2]/from PhD dissertation.

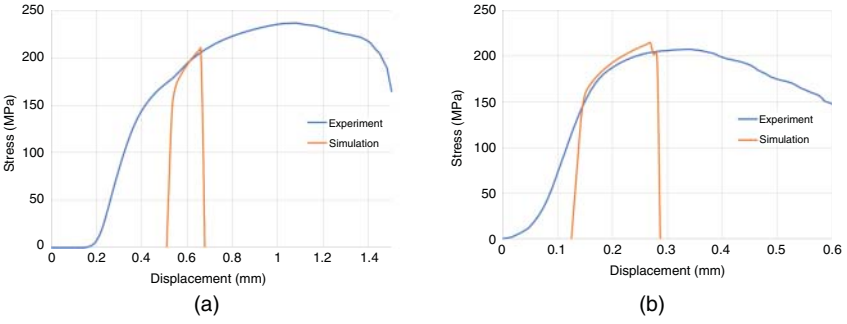

Figure 11.15 Comparison of shear test results between experiments and FE simulations of a full-sized (a) cuboid sample and (b) stepped sample. Source: Han [2]/from PhD dissertation.

The stress distribution map prior to the shear failure is shown in Figure 11.14. The stress is concentrated in the desired regions for both the cuboid and stepped samples. Simulated shear stress versus displacement curves are compared to experimental results for the cuboid and stepped samples in Figure 11.15. For the cuboid sample, the maximum shear stress is measured as 237.0 MPa and simulated as 210.0 MPa. For the stepped sample, the maximum shear stress is measured as 207.8 MPa and simulated as 214.8 MPa. The simulated maximum stress is close to the measured value for both cases. The simulated displacement is smaller than the measured displacement because the simulation assumes perfect sample geometry and alignment with the shear fixture as well as pure transverse shear during testing. However, in practice, geometries are not perfect, and small angle rotation and bending may happen simultaneously with transverse shear loading. Therefore, the measured displacement does not have a precise physical meaning with regard to the material properties of the sample. Similar to other transverse shear testing methods, this miniature shear method can provide a pretty close approximation of the shear strength using peak shear load. However, it is not the best tool to estimate the shear stress versus displacement curve. Of note, the initial slope of the simulated shear stress versus the

displacement curve remains constant since a perfect contact scenario is assumed. However, the initial slope of the experimental curve gradually increases from zero to a constant value, which may result from the initial engagement and contact between the shearing plates and the samples.

11.4.4 Application of the Shear Test to UAM Samples

Shear testing of the bulk Al 6061 T6 samples demonstrated the feasibility of this test method and the use of the stepped shape. However, the dimensions of the length L and the height H needed further optimization. It was expected that a shorter length would require a shorter traveling distance and be more accurate. However, this dimension is constrained by practical limits. Since the stepped samples are machined to final dimensions using CNC machining, the stepped parts would break off during machining if the length were too short. Thus, after a series of trials, the minimum length was found to be 1.42 mm (0.056 in.). It was speculated that a full-height stepped part of 3.25 mm tall would prevent sample rotation within the fixture during testing and provide a more accurate measurement. However, the full-height sample requires extra cost in time and material to make the UAM sample. Moreover, for certain materials such as steels, undesired cracking can occur as build height increases, which makes it difficult to build full-height samples under current processing conditions. To understand if build height affects the test results, shear samples of UAM-made Al 6061 were produced with short, middle, and tall heights, as shown in the schematics of Figure 11.16.

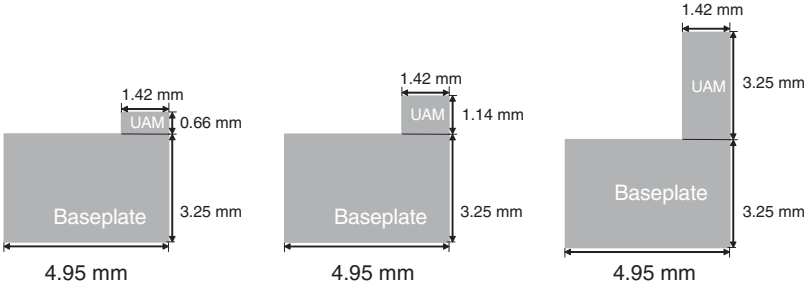

Figure 11.16 Schematic of (a) short height, (b) middle height, and (c) tall height shear samples with nominal dimensions. Source: Han [2]/from PhD dissertation.

Table 11.3 Process parameters used to weld Al 6061 H18 and carbon steel 4130.

Parameters	Al 6061 H18	Steel 4130
Normal force (N)	4000	6500
Vibration amplitude (μm)	35.0	30.0
Weld speed (mm/s)	85	21
Baseplate temperature (°C)	24	204

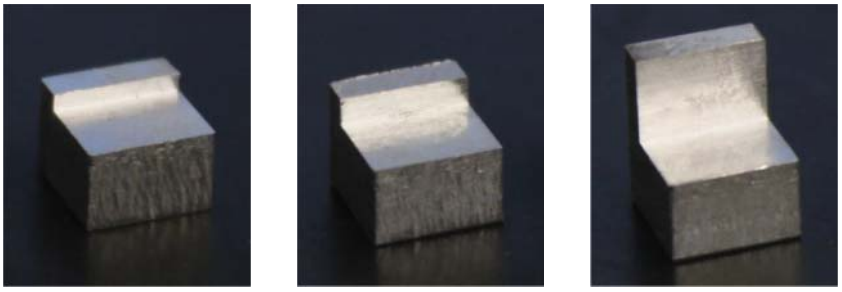

Figure 11.17 Machined shear samples of UAM Al 6061 H18 with (a) short, (b) middle, and (c) tall height dimensions as specified in Figure 11.16. Source: Han [2]/from PhD dissertation.

Table 11.4 Shear test results for UAM Al 6061 H18.

Sample	Shear strength of short height sample (MPa)	Shear strength of middle height sample (MPa)	Shear strength of tall height sample (MPa)
1	88.9	90.0	82.8
2	82.2	85.6	81.1
3	78.5	84.0	78.9
4	89.0	87.2	78.4
Average	84.7	86.7	80.3
Std	4.5	2.2	1.7

All samples were made using a Fabrisonic SonicLayer 4000 9 kW UAM system. Twenty-two layers of 0.152 mm (0.006 in.) thick, 25.4 mm (1 in.) wide Al 6061 H18 foils were welded onto a 6.35 mm (0.25 in.) thick Al 6061 T6 baseplate. Welding parameters used to make these builds are shown in Table 11.3. A 0.25 in. square end mill was used to extract the shear samples from the UAM build. Then, the shear samples were fixed in a high-precision vise and machined to their final dimensions. Images of the shear samples with varied height are shown in Figure 11.17. Four shear samples for each case were tested using an MTS C43.504 50 kN load frame. The shear test results are shown in Table 11.4. Despite the large height variation of 78%, the measured shear strength of UAM Al 6061 H18 varies less than 8%. These results have demonstrated the viability of using short-height stepped shear samples to characterize the shear strength of UAM samples.

To further expand the application of this shear test to the UAM steel domain, UAM 4130 steel builds were made using the parameters shown in Table 11.3. Nine layers of 0.127 mm (0.005 in.) thick, 25.4 mm (1 in.) wide annealed carbon steel 4130 foils were welded onto a 6.35 mm (0.5 in.) thick ASTM A36 carbon steel baseplate. Four shear samples with the dimensions of the middle height sample shown in Figure 11.16 were made and tested. The test results are shown in Table 11.5.

Table 11.5 Shear test results for UAM 4130.

Sample	Shear strength (MPa)
1	156.3
2	158.0
3	142.1
4	178.4
Average	158.7
Std	13.4

As presented, the low standard deviation (std) of 13.4 MPa demonstrates the validity of the data and indicates the viability of this method for testing different UAM materials.

11.5 Conclusions

Typical microstructural analyses, mechanical characterization methods, and hardness measurements for evaluating UAM welds have been presented in this chapter through case studies on UAM builds with Al and steel. Microstructural analyses with SEM and EBSD show that both bonded and unbonded areas of the UAM interface may have experienced high strain rate deformation. Post-weld heat treatment methods including HIP can increase the interfacial strength of UAM steel by reducing interfacial defects and inducing pearlite and martensite at the UAM steel interface. HIP treatment is proven to increase the overall hardness of UAM stainless steel 410 from 204 ± 7 HV to 240 ± 16 HV as a result of the creation of local pockets of martensite. According to nanohardness testing, the top of layer n is harder than the bottom of layer $n+1$. At the interface, there is an increase in hardness, which results from grain boundary strengthening. A custom shear test procedure is developed to characterize the mechanical strength of UAM samples. The shear test method was first validated with bulk cast Al of two configurations. The stepped shape samples give a 2.3% error compared to the reference shear strength of 207 MPa. Then, an FE model was developed to examine the influence of the shape and dimensions of shear test samples on the shear test results. The simulations agree with experimental measurements. Finally, this shear test method was applied to characterize UAM-fabricated steel and Al. The results also indicate that the height of shear samples has little effect on the measured shear strength.

References

1 Graff, K.F., Short, M., and Norfolk, M. (2010). Very high power ultrasonic additive manufacturing (VHP UAM) for advanced materials. *2010 International Solid Freeform Fabrication Symposium* (23 September 2010). University of Texas at Austin.

2 Han, T. (2020). *Ultrasonic Additive Manufacturing of Steel: Process, Modeling, and Characterization*. The Ohio State University.

3 Guo, H., Gingerich, M.B., Headings, L.M. et al. (2019). Joining of carbon fiber and aluminum using ultrasonic additive manufacturing (UAM). *Composite Structures* 208: 180–188.

4 Wolcott, P.J. and Dapino, M.J. (2017). Ultrasonic additive manufacturing. In: *Additive Manufacturing Handbook* (ed. A.B. Badiru, V.V. Valencia, and D. Liu), 275–298. CRC Press.

5 Hahnlen, R. and Dapino, M.J. (2014). NiTi–Al interface strength in ultrasonic additive manufacturing composites. *Composites Part B: Engineering* 59: 101–108.

6 Hehr, A. and Dapino, M.J. (2015). Interfacial shear strength estimates of NiTi–Al matrix composites fabricated via ultrasonic additive manufacturing. *Composites Part B: Engineering* 77: 199–208.

7 Schomer, J.J., Hehr, A.J., and Dapino, M.J. (2016). Characterization of embedded fiber optic strain sensors into metallic structures via ultrasonic additive manufacturing. In: *Sensors and Smart Structures Technologies for Civil, Mechanical, and Aerospace Systems 2016*, vol. 9803 (ed. J.P. Lynch), 587–596. SPIE.

8 Sridharan, N., Wolcott, P., Dapino, M., and Babu, S.S. (2016). Microstructure and texture evolution in aluminum and commercially pure titanium dissimilar welds fabricated using ultrasonic additive manufacturing. *Scripta Materialia* 117: 1–5.

9 Wolcott, P.J., Sridharan, N., Babu, S.S. et al. (2016). Characterisation of Al–Ti dissimilar material joints fabricated using ultrasonic additive manufacturing. *Science and Technology of Welding and Joining* 21 (2): 114–123.

10 Deng, Z., Gingerich, M.B., Han, T., and Dapino, M.J. (2018). Yttria-stabilized zirconia-aluminum matrix composites via ultrasonic additive manufacturing. *Composites Part B: Engineering* 151: 215–221.

11 Kuo, C.H., Sridharan, N., Han, T. et al. (2019). Ultrasonic additive manufacturing of 4130 steel using Ni interlayers. *Science and Technology of Welding and Joining* 24 (5): 382–390.

12 Hopkins, C.D., Wolcott, P.J., Dapino, M.J. et al. Optimizing ultrasonic additive manufactured Al 3003 properties with statistical modeling. *Journal of Engineering Materials and Technology* 134 (1): 011004.

13 Kong, C.Y., Soar, R.C., and Dickens, P.M. (2003). Characterisation of aluminium alloy 6061 for the ultrasonic consolidation process. *Materials Science and Engineering A* 363 (1–2): 99–106.

14 Sriraman, M.R., Babu, S.S., and Short, M. (2010). Bonding characteristics during very high power ultrasonic additive manufacturing of copper. *Scripta Materialia* 62 (8): 560–563.

15 Han, T., Kuo, C.H., Sridharan, N. et al. (2020). Effect of weld power and interfacial temperature on mechanical strength and microstructure of carbon steel 4130 fabricated by ultrasonic additive manufacturing. *Manufacturing Letters* 25: 64–69.

16 Han, T., Headings, L.M., Hahnlen, R., and Dapino, M.J. (2022). Effect of process parameters on interfacial temperature and shear strength of ultrasonic additive manufacturing of carbon steel 4130. *Journal of Manufacturing Science and Engineering* 144 (8): 084501.

17 Han, T., Kuo, C.H., Sridharan, N. et al. (2020). Effect of preheat temperature and post-process treatment on the microstructure and mechanical properties of stainless steel 410 made via ultrasonic additive manufacturing. *Materials Science and Engineering A* 769: 138457.

18 Shimizu, S., Fujii, H.T., Sato, Y.S. et al. (2014). Mechanism of weld formation during very-high-power ultrasonic additive manufacturing of Al alloy 6061. *Acta Materialia* 74: 234–243.

19 Lins, J.F., Sandim, H.R., Kestenbach, H.J. et al. (2007). A microstructural investigation of adiabatic shear bands in an interstitial free steel. *Materials Science and Engineering A* 457 (1–2): 205–218.

20 Levy, A., Miriyev, A., Sridharan, N. et al. (2018). Ultrasonic additive manufacturing of steel: method, post-processing treatments and properties. *Journal of Materials Processing Technology* 256: 183–189.

21 Sridharan, N., Gussev, M.N., Parish, C.M. et al. (2018). Evaluation of microstructure stability at the interfaces of Al-6061 welds fabricated using ultrasonic additive manufacturing. *Materials Characterization* 139: 249–258.

22 Uday, M.B., Ahmad-Fauzi, M.N., Noor, A.M., and Rajoo, S. (2016). Current issues and problems in the joining of ceramic to metal. In: *Joining Technologies* (ed. M. Ishak), 159. IntechOpen.

23 Kong, C.Y., Soar, R.C., and Dickens, P.M. (2004). Optimum process parameters for ultrasonic consolidation of 3003 aluminium. *Journal of Materials Processing Technology* 146 (2): 181–187.

24 de Freitas, S.T. and Sinke, J. (2014). Adhesion properties of bonded composite-to-aluminium joints using peel tests. *The Journal of Adhesion* 90 (5–6): 511–525.

25 Zhang, C., Deceuster, A., and Li, L. (2009). A method for bond strength evaluation for laminated structures with application to ultrasonic consolidation. *Journal of Materials Engineering and Performance* 18: 1124–1132.

26 Shih, C., Katoh, Y., Kiggans, J.O. et al. (2014). Comparison of shear strength of ceramic joints determined by various test methods with small specimens. In: *Ceramic Materials for Energy Applications IV: A Collection of Papers Presented at the 38th International Conference on Advanced Ceramics and Composites January 27–31, 2014 Daytona Beach, Florida*, vol. 35, 139–149. Hoboken, NJ: Wiley.

27 Iosipescu, N. (1967). New accurate procedure for single shear testing of metals. *Journal of Materials* 2: 537–566.

28 Roy, S., Bose, T., and Debnath, K. (2019). Behaviour of glass fiber-reinforced composite with delamination under Iosipescu shear test. *International Journal of Modern Manufacturing Technologies* 11: 119–125.

29 Shear strength of Al 6061 T6. http://asm.matweb.com/search/Speci_cMaterial.asp?bassnum=MA6061T6 (accessed 5 October 2020).

30 Smith, M. (2009). ABAQUS/Standard User's Manual, Version 6.9.